Sensitivity of Simulated Climate to Two Atmospheric Models: Interpretation of Differences between Dry Models and Moist Models

HE ZHANG

ICCES, Institute of Atmospheric Physics, Chinese Academy of Sciences, Beijing, China

MINGHUA ZHANG

ICCES, Institute of Atmospheric Physics, Chinese Academy of Sciences, Beijing, China, and School of Marine and Atmospheric Sciences, Stony Brook University, Stony Brook, New York

QING-CUN ZENG

ICCES, Institute of Atmospheric Physics, Chinese Academy of Sciences, Beijing, China

(Manuscript received 17 December 2011, in final form 14 September 2012)

ABSTRACT

The dynamical core of the Institute of Atmospheric Physics of the Chinese Academy of Sciences Atmospheric General Circulation Model (IAP AGCM) and the Eulerian spectral transform dynamical core of the Community Atmosphere Model, version 3.1 (CAM3.1), developed at the National Center for Atmospheric Research (NCAR) are used to study the sensitivity of simulated climate. The authors report that when the dynamical cores are used with the same CAM3.1 physical parameterizations of comparable resolutions, the model with the IAP dynamical core simulated a colder troposphere than that from the CAM3.1 core, reducing the CAM3.1 warm bias in the tropical and midlatitude troposphere. However, when the two dynamical cores are used in the idealized Held–Suarez tests without moisture physics, the IAP AGCM core simulated a warmer troposphere than that in CAM3.1. The causes of the differences in the full models and in the dry models are then investigated.

The authors show that the IAP dynamical core simulated weaker eddies in both the full physics and the dry models than those in the CAM due to different numerical approximations. In the dry IAP model, the weaker eddies cause smaller heat loss from poleward dynamical transport and thus warmer troposphere in the tropics and midlatitudes. When moist physics is included, however, weaker eddies also lead to weaker transport of water vapor and reduction of high clouds in the IAP model, which then causes a colder troposphere due to reduced greenhouse warming of these clouds. These results show how interactive physical processes can change the effect of a dynamical core on climate simulations between two models.

1. Introduction

The dynamical core of an atmospheric general circulation model (AGCM) refers to the formulation of the hydrodynamic equations of the atmosphere and the numerical algorithms to solve them. The governing equations among models may be different, depending on the purpose of the model applications, such as hydrostatic versus nonhydrostatic models. But even if the governing equations are the same, when formulated differently, the discretization methods can make them different. This is the case for the two dynamical cores used in this paper: one with transformed velocity as control variables of air motion by the finite-difference method [the dynamical core of the Institute of Atmospheric Physics (IAP) of the Chinese Academy of Sciences Atmospheric General Circulation Model, referred as the IAP core; Zhang 2009], and the other with the vorticity and divergence as control variables by the spectral method [the Community Atmosphere Model, version 3.1 (CAM3.1), developed by the National Center for Atmospheric Research (NCAR), referred as the CAM core; Collins et al. 2004]. In this paper, we include the treatment of diffusion from numerical sources and physical terms as part of the dynamical core.

Different numerical schemes have been used to solve the same atmospheric governing equations in different

Corresponding author address: Minghua Zhang, SoMAS, Stony Brook University, Stony Brook, NY 11794-5000.
E-mail: mzhang@notes.cc.sunysb.edu

modeling centers. Ideally, with sufficiently high resolution, these different numerical schemes should converge to each other. But resolution is always constrained by available computing resources. Therefore, improvement of dynamical cores has been an ongoing process in the climate modeling community. The robustness of a numerical scheme includes its accuracy, consistency, stability, conservation, and computational efficiency. Because of limited resolutions, the theoretical benefits of these measures may not be realized in practice.

Therefore, there is the need to understand and verify dynamical cores to assure the quality of model simulations (Williamson 2007). Several idealized cases have been designed to specifically test the numerical robustness of dynamical cores (Held and Suarez 1994; Boer and Denis 1997; Polvani et al. 2004; Jablonowski and Williamson 2006). These have been very valuable to understand the sensitivity of numerical solutions to different schemes and resolutions. Most of these tests are formulated without moist physics. But because numerical approximations are flow dependent, it is also important to understand the behavior of atmospheric dynamical cores in real settings of the atmosphere with moist physics.

The objective of this paper is to investigate the impact of the IAP AGCM dynamical core on simulated climate. We compared results from two models with the same physics package [the CAM3.1 physics package of Collins et al. (2004) and the dry physics of Held and Suarez (1994)], one using the IAP dynamical core (referred to as the IAP model), and the other using Eulerian spectral transform dynamical core of the CAM3.1 (referred to as the CAM model). We report how the interactive physical parameterizations change the sensitivities of simulated climate to the dynamical cores. To our knowledge, no previous study has reported the causes of different sensitivities between the dry and moist models.

We wish to point out that the two dynamical cores used in this paper represent two traditional methods (finite difference vs spectral) in climate models. Large advances have been made in recent years on the front of dynamical cores, including the formulation of equations, flexibilities of grids, discretization methods, and computational efficiency (e.g., Taylor et al. 2008; Baba et al. 2010; Donner et al. 2011; Ringler et al. 2011). It is the authors' hope that results from the present study will also be useful to interpret the sensitivities of model results with more sophisticated dynamical cores.

This paper is organized as follows. Brief descriptions of the IAP AGCM dynamical core and the experiments are given in section 2. Section 3 compares the simulations of temperature and general circulation between IAP AGCM4.0 and CAM3.1. Results from the dry

models and aquaplanet tests are also presented, along with interpretation of the sensitivities. The last section contains a summary.

2. Model description and experimental setup

a. IAP dynamical core

The fourth version of the IAP AGCM has evolved from several earlier versions that have been documented in the literature (Zeng et al. 1989; Bi 1993; Liang 1996; Zuo 2003; Zhang 2009). It has been used to simulate atmospheric circulations and climate, including summer precipitation, monsoons, and spring dust storms (e.g., Zeng et al. 1997; Lin and Zeng 1997; Xue et al. 2001; Chen et al. 2004).

For the purpose of the present study, only the dynamical core is described. The model uses a finite-difference scheme with a terrain-following σ coordinate (Phillips 1957). A latitude–longitude grid with Arakawa's C grid staggering is used in the horizontal discretization (Arakawa and Lamb 1977). The horizontal grid structure was initially adapted from the Oregon State University two-layer model (Ghan et al. 1982), which can be further traced to the model at the University of California at Los Angeles (Arakawa and Lamb 1977). However, the formulation of the governing equations and the finite-difference schemes are different in the IAP model, which contain several novel features and these are described here.

First, the model equations are based on the baroclinic primitive equations with subtraction of standard stratification. The standard stratification is characterized by state variables $\tilde{T}(p), \tilde{\phi}(p)$ and $\tilde{p}_s(\theta, \lambda)$, which satisfy the following equations:

$$\begin{cases} R\tilde{T}(p) = -p \dfrac{d\tilde{\phi}(p)}{dp} \\ \tilde{p}|_{z=\tilde{z}_s(\theta,\lambda)} \equiv \tilde{p}_s(\theta,\lambda) \end{cases}, \quad (1)$$

where T is the temperature, $\phi = gz$ is the geopotential, z is the height, g is the gravity acceleration, p is the pressure, p_s is the surface pressure, θ is the colatitude, λ is the longitude, $\tilde{z}_s$ is the elevation of the earth's surface, and the "tilde" denotes the "standard atmosphere." With the standard atmosphere removed, the controlling equations solve the perturbation fields denoted by the prime:

$$\begin{cases} T'(\theta,\lambda,p,t) = T(\theta,\lambda,p,t) - \tilde{T}(p) \\ \phi'(\theta,\lambda,p,t) = \phi(\theta,\lambda,p,t) - \tilde{\phi}(p) \\ p'_{sa}(\theta,\lambda,t) = p_s(\theta,\lambda,t) - \tilde{p}_s(\theta,\lambda) \end{cases}. \quad (2)$$

The purpose of subtracting the standard stratification in the dynamical core is to reduce truncation errors, especially over regions of high terrain such as the Tibetan Plateau. The subtraction of a hydrostatic background state is also used in other models (Tomita and Satoh 2004; Giraldo and Restelli 2008).

Second, the IAP model conserves total available energy [sum of kinetic energy, the available potential energy, and the available surface potential energy, see details in Eq. (12)] rather than total energy. To facilitate the numerical design, it therefore used the following variable substitution, referred to as the IAP transform:

$$\begin{cases} (U, V, \Phi) \equiv (Pu, Pv, PRT'/b) \\ P \equiv \sqrt{p_{es}/p_0}, \quad p_{es} = p_s - p_t \end{cases}, \quad (3)$$

where $p_t = 2.2$ hPa is the pressure at the model top layer; $p_0 = 1000$ hPa; and $b = 87.8$ m s^{-1} is the approximate value of $\tilde{C}_0^2$, which is the characteristic velocity of gravity wave propagation of the standard atmosphere determined by $\tilde{C}_0^2 = R(\kappa \tilde{T} - d\tilde{T}/d\ln p)$, where $\kappa = R/c_p$; R is the gas constant for dry air; and c_p is the specific heat of dry air at constant pressure. After the subtraction of standard stratification, with the IAP transform and the vertical coordinate $\sigma \equiv (p - p_t)/p_{es}$, the dynamical core can be written as

$$\begin{cases} \dfrac{\partial U}{\partial t} = -\sum_{m=1}^{3} L_m(U) - P_\lambda - f^*V + PF_u \\[2ex] \dfrac{\partial V}{\partial t} = -\sum_{m=1}^{3} L_m(V) - P_\theta + f^*U + PF_v \\[2ex] \dfrac{\partial \Phi}{\partial t} = -\sum_{m=1}^{3} L_m(\Phi) + (1 - \delta_p)[(\tilde{C}_0^2/b) + (\varepsilon\kappa\Phi/P)][\Omega^{(1)} + \Omega^{(2)}] + PRT'F_T/b \\[2ex] \dfrac{\partial}{\partial t}\left(\dfrac{p'_{sa}}{p_0}\right) + D(P) + \dfrac{\partial P^2\dot{\sigma}}{\partial \sigma} = \dfrac{1}{p_0}\nabla \cdot \left(\tilde{\rho}_{sa}k_{sa}\nabla\dfrac{p'_{sa}}{\tilde{\rho}_{sa}}\right) \\[2ex] \dfrac{\partial \phi'}{\partial \sigma} = -\dfrac{p_{es}}{p}RT' \end{cases}, \quad (4)$$

where $\delta_p \equiv p_t/p$, f^* is determined by $f^* = 2\Omega\cos\theta + u\cot\theta/a$ with a as the earth radius, Ω is the angular velocity of the earth rotation, $\tilde{\rho}_{sa} = \tilde{p}_s/R\tilde{T}_s$ is the density of the standard atmosphere at the surface, $k_{sa} = 0.1$ is the dissipation coefficient, and $\dot{\sigma}$ is the vertical velocity on σ level. Here ε is 0 with the standard stratification approximation. If it is set to 1, the set of equations becomes the same as the primitive equations that are commonly used. The L_1 and L_2 are the horizontal advection operators and L_3 is the vertical convection operator, which are defined by

$$\begin{cases} L_1(F) \equiv \dfrac{1}{2a\sin\theta}\left(2\dfrac{\partial Fu}{\partial \lambda} - F\dfrac{\partial u}{\partial \lambda}\right) \\[2ex] L_2(F) \equiv \dfrac{1}{2a\sin\theta}\left(2\dfrac{\partial Fv\sin\theta}{\partial \theta} - F\dfrac{\partial v\sin\theta}{\partial \theta}\right). \\[2ex] L_3(F) \equiv \dfrac{1}{2}\left(2\dfrac{\partial F\dot{\sigma}}{\partial \sigma} - F\dfrac{\partial \dot{\sigma}}{\partial \sigma}\right) \end{cases} \quad (5)$$

The pressure gradient terms are calculated according to the following formulas:

$$\begin{cases} P_\lambda = P\dfrac{\partial \phi'}{a\sin\theta\partial \lambda} + \dfrac{b\Phi(1 - \delta_p)}{p_{es}}\dfrac{\partial p_{es}}{a\sin\theta\partial \lambda} \\[2ex] P_\theta = P\dfrac{\partial \phi'}{a\partial \theta} + \dfrac{b\Phi(1 - \delta_p)}{p_{es}}\dfrac{\partial p_{es}}{a\partial \theta} \end{cases} \quad (6)$$

where terms $\Omega^{(1)}$, $\Omega^{(2)}$, and $D(P)$ are determined by

$$\begin{cases} \Omega^{(1)} \equiv \dfrac{P\dot{\sigma}}{\sigma} - \dfrac{1}{P}\left[D(P) + \dfrac{\partial P^2\dot{\sigma}}{\partial \sigma}\right] \\[2ex] \Omega^{(2)} \equiv \dfrac{U}{p_{es}}\dfrac{\partial p_{es}}{a\sin\theta\partial \lambda} + \dfrac{V}{p_{es}}\dfrac{\partial p_{es}}{a\partial \theta} \\[2ex] D(P) \equiv \dfrac{1}{a\sin\theta}\left(\dfrac{\partial PU}{\partial \lambda} + \dfrac{\partial PV\sin\theta}{\partial \theta}\right) \end{cases}. \quad (7)$$

The F_u, F_v, and F_T are the horizontal diffusion operators, and are determined by

$$\begin{cases} F_u \equiv \dfrac{1}{\rho}\left[\dfrac{1}{a\sin\theta}\dfrac{\partial}{\partial\lambda}(\rho K_{\mathrm{MH}}D_T) + \dfrac{1}{a}\dfrac{\partial}{\partial\theta}(\rho K_{\mathrm{MH}}D_S)\right] \\[2mm] F_v \equiv \dfrac{1}{\rho}\left[\dfrac{1}{a\sin\theta}\dfrac{\partial}{\partial\lambda}(\rho K_{\mathrm{MH}}D_S) - \dfrac{1}{a}\dfrac{\partial}{\partial\theta}(\rho K_{\mathrm{MH}}D_T)\right] \\[2mm] F_T \equiv \dfrac{1}{\rho}\dfrac{1}{a^2\sin\theta}\left[\dfrac{1}{\sin\theta}\dfrac{\partial}{\partial\lambda}\left(\rho K_{\mathrm{TH}}\dfrac{\partial T}{\partial\lambda}\right) + \dfrac{\partial}{\partial\theta}\left(\rho K_{\mathrm{TH}}\sin\theta\dfrac{\partial T}{\partial\theta}\right)\right] \end{cases},$$

$$(8)$$

where

$$K_{\mathrm{TH}} = K_{\mathrm{MH}} = 2K_{\mathrm{dif}}^2(a\Delta\lambda\sin\theta)^2\sqrt{D_T^2 + D_S^2}, \quad (9)$$

$$D_T \equiv \frac{1}{a\sin\theta}\left[\frac{\partial u}{\partial\lambda} - \frac{\partial}{\partial\theta}(v\sin\theta)\right], \quad (10)$$

$$D_S \equiv \frac{1}{a\sin\theta}\left[\frac{\partial v}{\partial\lambda} + \frac{\partial}{\partial\theta}(u\sin\theta)\right]. \quad (11)$$

The K_{dif} is a proportionality constant that is set to 0.1.

The advantage of using the IAP transform is that the conservation of the sum of kinetic energy E_k, the available potential energy E_{ep}, and the available surface potential energy E_{es}, is conserved. They are written as

$$\begin{cases} E_k = \dfrac{p_0}{2g}\displaystyle\int_0^1\int_0^{2\pi}\int_0^{\pi}(U^2 + V^2)a^2\sin\theta\,d\theta\,d\lambda\,d\sigma \\[3mm] E_{\mathrm{ep}} = \dfrac{p_0}{2g}\displaystyle\int_0^1\int_0^{2\pi}\int_0^{\pi}\Phi^2 a^2\sin\theta\,d\theta\,d\lambda\,d\sigma \\[3mm] E_{\mathrm{es}} = \dfrac{1}{2g}\displaystyle\int_0^{2\pi}\int_0^{\pi}\dfrac{R\tilde{T}_s}{p_s}(p'_{\mathrm{sa}})^2 a^2\sin\theta\,d\theta\,d\lambda \end{cases}, \quad (12)$$

where $\partial(E_k + E_{\mathrm{ep}} + E_{\mathrm{es}})/\partial t = 0$ is in its differential form under the standard stratification approximation of $\varepsilon = 0$.

The central difference scheme is used to discretize the terms on the right-hand sides of Eqs. (4) with Arakawa's C grid. Two calculations are applied in the model to alleviate the reduction of the physical grid spacing problem in high latitudes. Poleward of $\pm 70°$, Fourier filtering is used on the tendencies of $U, V, \Phi, p'_{\mathrm{sa}}$ to damp the short longitudinal waves following Umscheid and Sankar-Rao (1971), which happen to be high-frequency waves as well. Between $\pm 30°$ and $\pm 90°$, we discretize $\partial F/\partial\lambda$ by

$$\left(\frac{\partial F}{\partial\lambda}\right)_{i,j} = \alpha_j\frac{F_{i+(1/2),j} - F_{i-(1/2),j}}{\Delta\lambda} + \beta_j\frac{F_{i+(3/2),j} - F_{i-(3/2),j}}{3\Delta\lambda},$$

$$(13)$$

where the subscript i and j denote the ith and the jth grid points for longitudinal and latitudinal direction,

respectively. The α_j and β_j are coefficients dependent on latitudes and satisfy $\alpha_j + \beta_j = 1$. The β_j increases linearly from 0 at $\pm 30°$ to 1 at $\pm 90°$ (Zhang et al. 2009). Furthermore, we split the model in Eqs. (4) to integrate the advection terms [e.g., $\sum_{m=1}^{3}L_m(U)$] with a time step of 600 s and the inertia–gravity wave terms (e.g., $P_\lambda + f^*V$) with a time step of 200 s to economize CPU time with the horizontal resolution 1.4° (latitude) by 1.4° (longitude).

The nonlinear iterative time integration method described in Zuo et al. (2004) is used in the model. For simplicity, the equation $\partial F/\partial t + A(F) = 0$ is considered here, where A is a nonlinear operator. The integration from time n to time $n + 1$ follows:

$$F_{(1)}^{n+1} - F^n = \Delta t A(F^n)$$

$$F_{(2)}^{n+1} - F^n = \Delta t A[F_{(1)}^{n+1}]$$

$$F_{(3)}^{n+1} - F^n = \Delta t A\left[\frac{F_{(2)}^{n+1} + F^n}{2}\right]$$

$$\vdots$$

$$F_{(2m)}^{n+1} - F^n = \Delta t A[F_{(2m-1)}^{n+1}]$$

$$F_{(2m+1)}^{n+1} - F^n = \Delta t A\left[\frac{F_{(2m)}^{n+1} + F^n}{2}\right], \quad (14)$$

where $m = 1, 2, 3, \ldots$. For the current version of the IAP AGCM, the number of steps in the multistep algorithm is 3 ($m = 1$) (Zuo et al. 2004).

The horizontal diffusion is a ∇^2 form [Eq. (8)] similar to Washington and Kasahara (1970). The semi-Lagrangian method (Williamson and Rasch 1989) is used to solve the water vapor continuity equation. The same CAM3.1 physical package [see Collins et al. (2004) in details], without any empirical physics parameters tuning, is adopted in this study. The time step for physics is 1200 s, and the physics package is coupled to the dynamics using the process-split method described in Williamson (2002). In our simulations, the vertical levels and their locations are set approximately the same as CAM3.1 (about 2.2 hPa at the top of the model with 26 levels). The IAP model uses 256 grid points in longitudes and 128 grid points in latitudes with equidistant grid spacing, which has approximately the same number of grids in the T85 spectral resolution (256 longitudinal grids and 128 latitudinal grids with the Gaussian grid) of CAM3.1. As pointed out in Williamson (2008), however, T85 spectral resolution is equivalent to about 1° resolution in the finite-volume dynamical core. We, therefore,

also carried out simulations using 1° resolutions in a sensitivity experiment.

b. The CAM3.1 Eulerian spectral transform dynamical core

The CAM3.1 has three different dynamical cores as well as different horizontal resolutions. The standard Eulerian spectral-transform method with horizontal resolution T85 is used in this paper. The horizontal diffusion is a linear ∇^2 form with coefficient $K^{(2)} = 2.5 \times 10^5$ m^2 s^{-1} in the top three layers of the model and a linear ∇^4 form with coefficient $K^{(4)} = 1.0 \times 10^{15}$ m^4 s^{-1} elsewhere. The time step for the dynamical core is 600 s and that for the physics package is 1200 s. Other details about CAM3.1 are given in Collins et al. (2004). The main differences with the IAP dynamical core include the following: 1) vorticity and divergence as prognostic variables, 2) spectral representation of all linear terms and calculation of the nonlinear terms in gridpoint space, 3) harmonic and biharmonic horizontal diffusion versus harmonic diffusion in the IAP core, 4) conservation of total energy by an energy fixer instead of conservation of available potential energy, and 5) no subtraction of standard stratification as in the IAP model.

c. Experimental setup

The IAP AGCM4.0 and CAM3.1 are both integrated for 17 years with the same physics package, and the boundary and initial conditions are interpolated from the same input data. Averages of the simulations over the last 15 years are presented. The SST and sea ice datasets are climatological monthly datasets from blended products that combined the global Hadley Centre Sea Ice and Sea Surface Temperature (HadISST) dataset (Rayner et al. 2003) for years up to 1981 and the Smith–Reynolds EOF dataset (Reynolds et al. 2002) post-1981. The concentrations of greenhouse gases are held constant at their levels in 1990, with CO_2 concentration of 355 ppmv. The primary sources of the validation data are the National Centers for Environmental Prediction–National Center for Atmospheric Research (NCEP–NCAR) reanalysis (Kalnay et al. 1996) and the European Centre for Medium-Range Weather Forecasts Re-Analysis Interim (ERA-Interim; Dee et al. 2011). Both the model results and reanalysis data are truncated to T42 and 17 pressure levels for direct comparison. ERA-Interim reanalysis is used in the eddy transport calculations, since recent studies suggest that the ERA-Interim has better quality than the NCEP–NCAR reanalysis and the eddy transport is weaker in the NCEP–NCAR reanalysis than that in the ERA-Interim reanalysis (Decker et al. 2012). The mean climatological fields of the atmospheric state variables are, however, similar in the two reanalysis products.

3. Results

a. Temperature and general circulation from climate simulations

We have examined a suite of atmospheric fields from the IAP model by using the Atmospheric Model Working Group (AMWG) diagnostics package developed at NCAR (http://www.cgd.ucar.edu/cms/rneale/tools/amwg_mean_diagnostics.html). The overall performance of the model IAP is described in Zhang (2009). In this paper, we only focus on the differences between the simulations of the IAP model and the CAM3.1.

Figures 1a,b show the deviation of the zonally averaged temperature from the NCEP–NCAR reanalysis in the models. The differences between the IAP model and the CAM3.1 simulations are shown in Fig. 1c. Shading indicates differences judged statistically significant at the 0.05 level for a Student's t test based on 15 annual-mean simulations. As in most AGCMS (Boer et al. 1992), there exists a notable cold bias near the polar tropopause in both models. Moreover, the CAM3.1 has a warm bias throughout most of the troposphere. This warm bias is systematically reduced in the model with the IAP dynamical core, especially in the tropics and midlatitudes, where the simulated temperature with the IAP core is colder than that in the CAM3.1 by more than 2 K, and this colder difference is statistically significant. Poleward of 50°N and 50°S, the IAP model simulated warmer troposphere than CAM. Since the IAP model used polar filters but the CAM model did not, it is difficult to trace the causes of the differences at high latitudes. We, therefore, focus on the simulation differences in low and midlatitudes.

The distribution of the zonal wind has traditionally been one of the fundamental measures of climate simulations. It is closely linked geostrophically to the temperature by the thermal wind relation. Figures 2a–c show that both models simulated the main features of the observed zonal winds, including the westerly jet cores located near 200 hPa over the midlatitudes of both hemispheres, and the tropical easterlies in the lower and middle troposphere as well as in the stratosphere. The two models overestimated the intensity of the westerly jet in both hemispheres (Figs. 2d,e). This overestimation, however, is reduced by about half in the IAP model relative to CAM3.1. The jets in CAM3.1 are stronger than in the NCEP–NCAR reanalysis by 4–6 and 6–8 m s^{-1} in Northern Hemisphere (NH) and Southern Hemisphere (SH), respectively, while the corresponding biases in the IAP model are about 2 and 4 m s^{-1}. This can be more clearly seen in the difference figure between the two models (Fig. 2f).
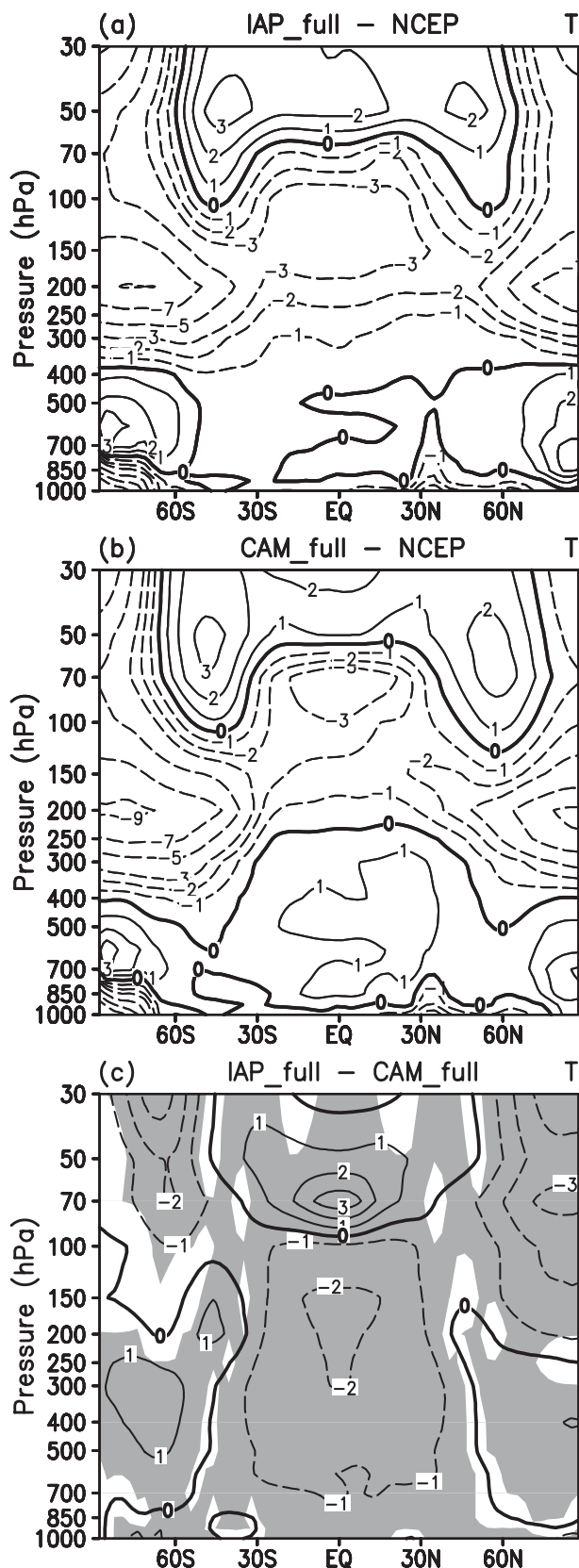
Transports of heat and momentum by eddies are important mechanisms to establish the general circulation and maintain the energy balance as well as angular momentum conservation of the atmosphere. The observed climatological annual mean of zonally averaged transient eddy heat fluxes in Fig. 3c shows two peaks of poleward heat fluxes in the lower and upper troposphere at midlatitudes. Both simulations with the IAP model (Fig. 3a) and the CAM3.1 (Fig. 3b) capture these two peak patterns well. The ERA-Interim reanalysis annual mean transient eddy heat flux $\overline{v'T'}$ is calculated from 10-yr 6-hourly data; the model $\overline{v'T'}$ is calculated by

$$\overline{v'T'} = \overline{vT} - \overline{v}\,\overline{T} \qquad (15)$$

from instantaneous data, where the bar denotes the monthly mean and the prime denotes the deviation from the mean. Figure 3 indicates that the general pattern of the transient eddy heat fluxes is simulated well in both IAP model and CAM3.1, but the strength is too strong in the models. Relative to the CAM3.1, Fig. 3d indicates weaker poleward heat transport above 500 hPa in the IAP model. In the calculation of the eddy transport in the models, we have first interpolated the model data from model levels to pressure levels by linear interpolation using pressure; we then calculated time-mean transport, which is further interpolated to T42 resolution and zonally averaged. The interpolation and remapping may affect the magnitudes of the eddy transport, but these effects can only weaken the model values, so stronger eddy transports in the models are likely affected by the calculation procedure.

The weaker eddies in the IAP model can be more clearly seen in the eddy momentum transport of Fig. 4. Since spectral models nominally represent a higher resolution than gridpoint models with the same number of grid points (Williamson 2008), there is the possibility that the more diffusive simulation in the IAP model is due to the "lower" resolution. We therefore conducted an additional simulation of the IAP AGCM4.0 with a finer resolution of 1° × 1° and compared the results against the CAM3.1 with T85 in Fig. 5. It can be seen that the eddy activities are also weaker in the finer resolution IAP AGCM4.0 compared to the CAM3.1. An

←

FIG. 1. The biases of zonally averaged 15-yr annual mean temperature from (a) IAP and (b) CAM simulations with contrast to the NCEP–NCAR reanalysis data, and (c) their difference (IAP − CAM). Contour intervals are 1 K between −3 and +3 K but 2 K beyond in (a),(b) and 1 K in (c). Shaded areas are statistically significant at the 0.05 level from the Student's t test in this and other figures.
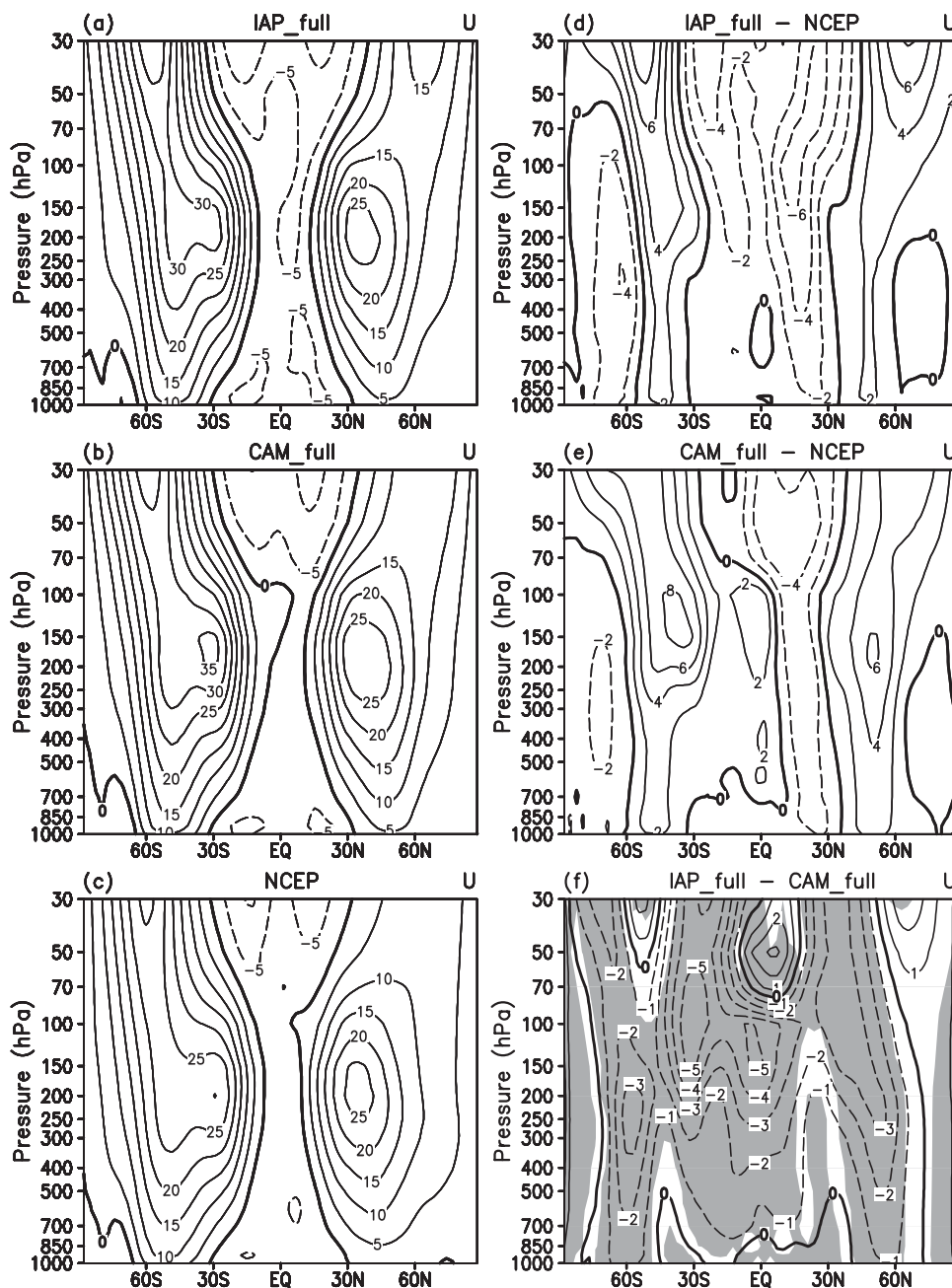
FIG. 2. Zonally averaged 15-yr annual mean zonal wind from (a) IAP, (b) CAM, (c) NCEP–NCAR reanalysis data, the biases of (d) IAP and (e) CAM with contrast to NCEP–NCAR reanalysis data, and (f) the difference of the two simulations (IAP − CAM). Contour intervals are 5 m s^{-1} in (a)–(c), 2 m s^{-1} in (d),(e), and 1 m s^{-1} in (f).

additional experiment was conducted in which the CAM resolution is degraded from T85 to T42. We found similar difference between the IAP model and the CAM.

We pointed out that the IAP model and the CAM model have different horizontal diffusion schemes, which may impact on kinetic energies. Figure 6 shows the 250-hPa eddy kinetic energy spectra form CAM3.1

simulations with T85 and IAP AGCM4.0 simulations with resolutions of 1.4° × 1.4° and 1° × 1°. The spectra are calculated from climate simulations and are averaged over 100 samples separated by 24 h. We found that the eddy kinetic energy from the CAM is larger than the IAP model for total wavenumber $n < 10$. This is consistent with the weaker eddies in the IAP model in
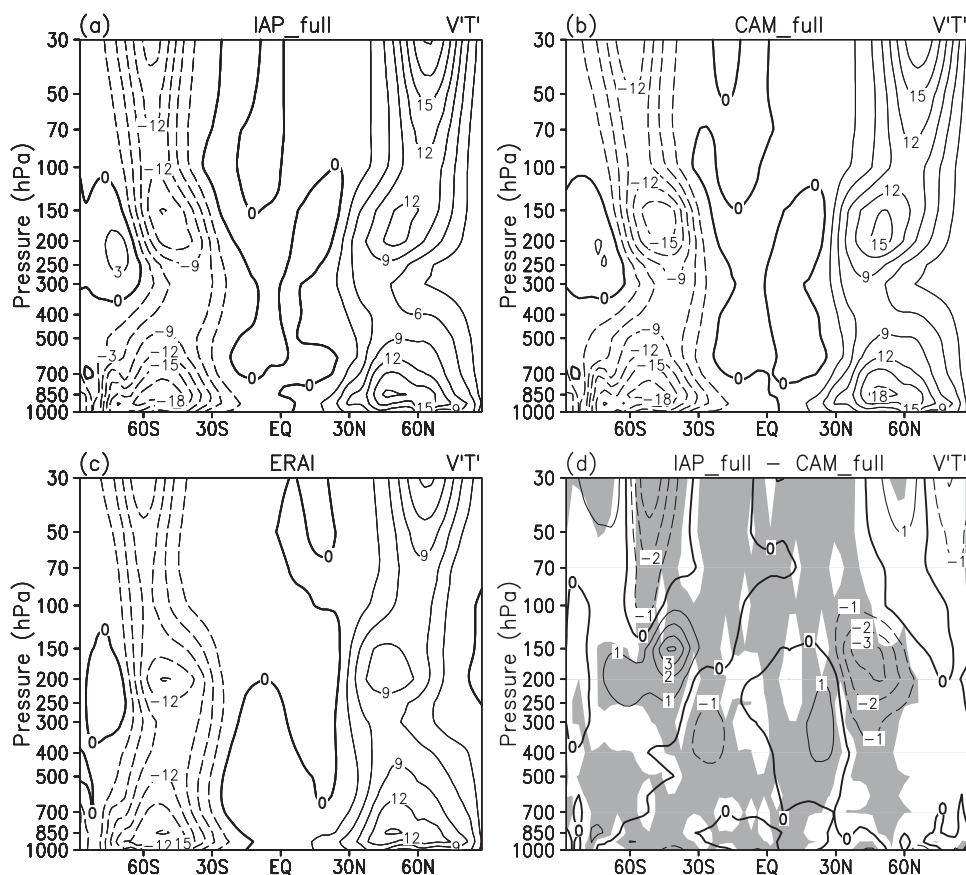
FIG. 3. (a),(b) As in Fig. 2, but for transient eddy heat flux; (c) ERA-Interim reanalysis data; and (d) the difference of the two simulations (IAP − CAM). Contour intervals are 3 K m s^{-1} in (a)–(c) and 1 K m s^{-1} in (d).

Fig. 5b. For wavenumber $10 < n < 60$, the three spectra are very close to each other and all have a slop close to n^{-3}, in agreement with the theories of 2D and quasi-geostrophic turbulence (Charney 1971). Above $n > 60$, the spectra form the CAM model descends faster than the IAP model, most likely caused by higher-order diffusion from the ∇^4 form in the CAM model.

b. Held–Suarez test

To contrast with the model with full physics, we next examine the impact of the dynamical core without moist physics by using the Held and Suarez (1994) experiment, hereafter referred to as H–S. The thermal forcing is Newtonian relaxation to a specified temperature field of varying time scale with latitudes and pressure. The momentum forcing is a sink represented by Rayleigh friction in the lower troposphere. The atmosphere is integrated without moist processes, topography, land–sea contrast, and seasonal or diurnal cycle.

The initial condition is not important in the H–S test, since after several months of integration, the prescribed forcing drives the model dynamics to quasi-equilibrium state that is independent of the initial state. In this paper, the integration of the model with the IAP dynamical core (referred to as IAP core) started from the same initial condition as for the full model run. The CAM3.1 (referred to as CAM core) started from an earlier run of a lower-resolution T42 simulation. Both models were integrated for 1220 days. By discarding 200 days, the remaining 1020 days are divided to 17 periods of 60 days. Independent 40 day samples are obtained by discarding 20 days in each period. The time-mean fields and statistics are taken from the 17 samples.

Figure 7 shows zonally averaged 17-period mean temperature from the H–S tests with the IAP core and CAM core and their difference with statistical significance Student's t test. The major features of the real atmosphere are reproduced with the idealized forcing as what is expected. What is not expected, however, is that simulated troposphere in the IAP core is generally warmer than that in the CAM core, which is opposite to the results found in the climate simulations shown in
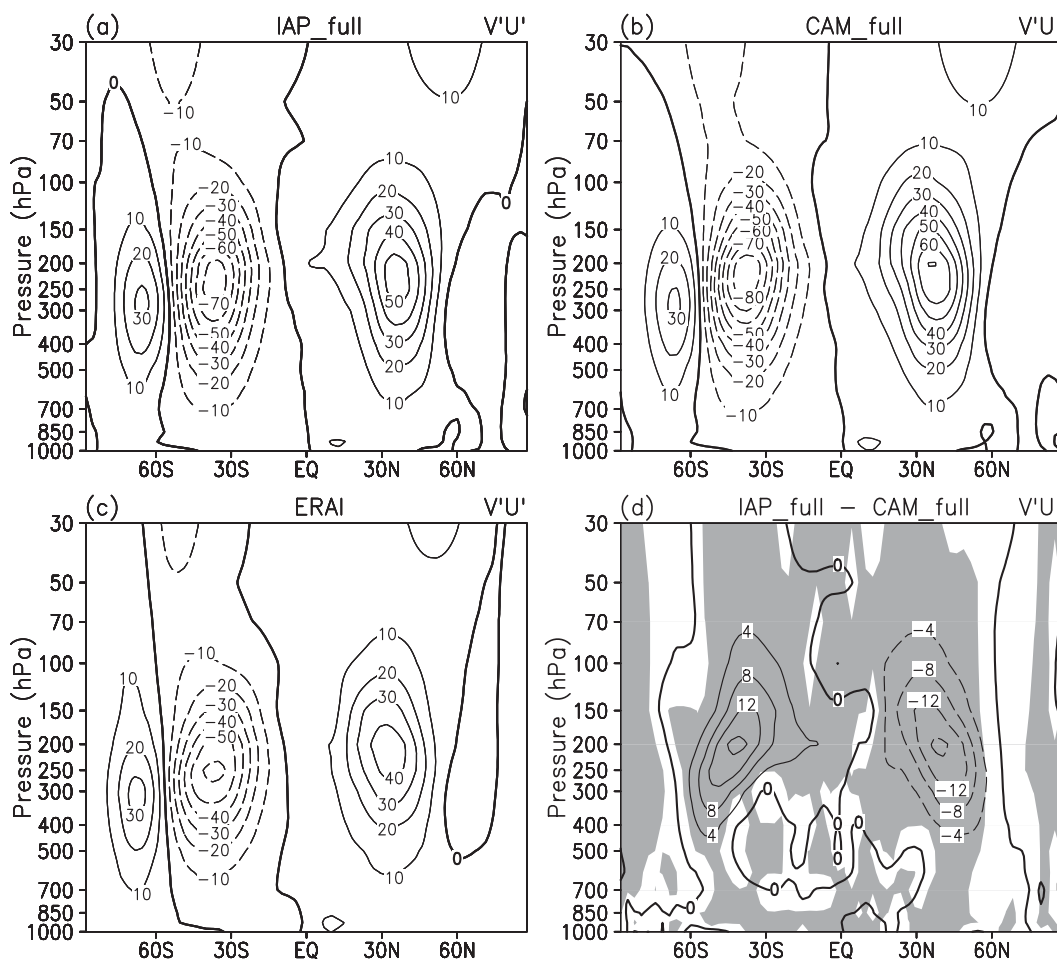
FIG. 4. (a)–(d) As in Fig. 3, but for transient eddy momentum flux. Contour intervals are 10 m² s⁻² in (a)–(c) and 4 m² s⁻² in (d).

Fig. 1c. Associated with the warmer troposphere, the simulated westerly jets in the IAP core are slightly stronger than those from the CAM core (Fig. 8). This difference is also opposite to that in the climate simulations, in which the jets are weaker in the IAP model.

The distribution of simulated eddy heat flux from H–S tests is presented in Fig. 9. The patterns of eddy heat fluxes of the H–S tests are similar to the climate simulations with two peaks located in lower and upper troposphere, respectively. The difference between the two dynamical cores in Fig. 9c is similar to the climate simulations in Fig. 3d, with weaker heat transports in the IAP core. The eddy momentum fluxes simulated by two cores are shown in Fig. 10. Consistent with the full models, the values of the maxima are smaller in the IAP core. Therefore, the IAP model simulated weaker eddy activities in both models with full physics and in the dry model than those in CAM3.1, yet the IAP model simulated colder troposphere in the full physics model but warmer troposphere in the dry model than CAM3.1.

c. Aquaplanet test

Because the IAP model and the CAM3.1 model differ in their handling of the topography (the IAP model used the deviation of surface pressure from the standard stratification), we conducted aquaplanet experiments to exclude the possible impact of the different treatment of surface topography in the full models. The results from the aquaplanet tests by IAP AGCM4.0 (hereafter IAP aqua) and by CAM3.1 (hereafter CAM aqua) will be compared with the results from real climate simulations and from H–S tests.

As in Neale and Hoskins (2000), the aquaplanet simulations with their control SST distribution by the two models are integrated for 40 months, with the last 36 months used for the analysis. For simplicity, only the differences of the two models are given here (Fig. 11). Relative to the CAM aqua, the following four features can be identified: 1) the IAP aqua simulated a colder troposphere (Fig. 11a), 2) the westerly jet is weaker and

FIG. 6. The 250-hPa eddy kinetic energy spectra as a function of total wavenumber n in climate simulations from the IAP model with resolution $1° \times 1°$ (dashed line), $1.4° \times 1.4°$ (dotted line), and from CAM with T85 (solid line). Straight line in the top-right-hand corner has slope of -3.
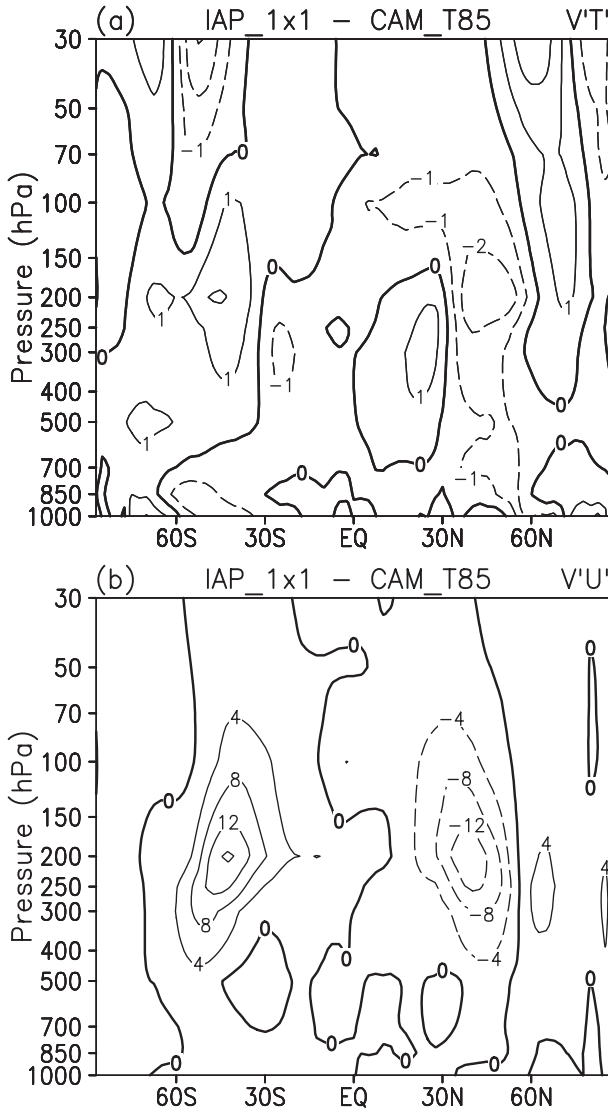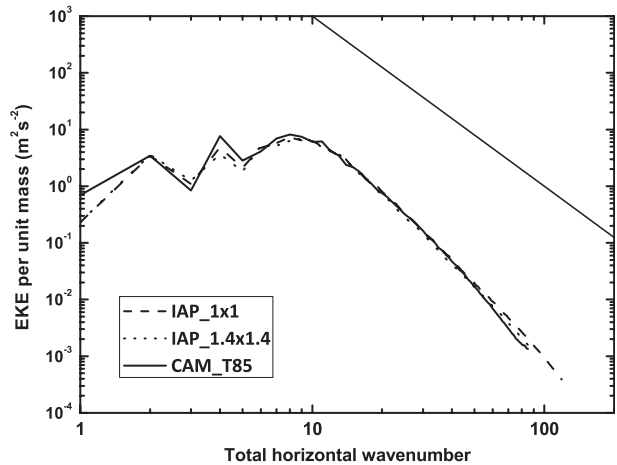

FIG. 5. Differences of (a) zonally averaged 5-yr annual mean transient eddy heat flux and (b) momentum flux from the climate simulations between the IAP AGCM4.0 with resolution $1° \times 1°$ and the CAM3.1 with resolution T85 (IAP $-$ CAM). Contour intervals are (a) 1 K m s^{-1} and (b) 4 m^2 s^{-2}.

displaced equatorward in the IAP aqua (Fig. 11b), 3) the poleward eddy heat transport at midlatitudes around 45°N and 45°S is weaker in the IAP aqua (Fig. 11c), and 4) the momentum transport is weaker in the IAP aqua (Fig. 11d). The first two features are consistent with the differences between the two models with full physics, but opposite to those in the H–S tests. The last two features are consistent among all experiments.

These results confirm that the IAP dynamical core simulates less energetic eddies in all experiments. It would be more satisfying if we can definitively attribute the weaker eddies in the IAP model to the specifics of

a numerical scheme relative to the CAM3.1. Such attribution, however, is known to be very difficult. Previous studies have also shown large sensitivities of eddy kinetic energy to dynamical cores (Wan et al. 2008). The causes of these sensitivities can be due to possible factors such as the formulation of the controlling equations, the discretization method, and horizontal diffusion processes. The second-order centered difference scheme in the IAP core is likely an important factor. Held and Suarez (1994), after comparing a spectral core and fourth-order finite-difference dynamical core, also noted that when a fourth-order version of the finite-difference dynamical core was replaced by a second-order version, their model produced quite different simulations with much weaker eddies. With this sensitivity in mind, in the following, we focus on why weaker eddies in the IAP model caused colder troposphere in the model with full physics relative to CAM3.1, but warmer troposphere in the dry model.

d. Interaction between moist physics and dynamics

To aid the discussion, we write the zonally averaged atmospheric thermodynamic equation as

$$\frac{\partial \overline{\theta}}{\partial t} = -\frac{1}{a \cos\varphi} \frac{\partial \cos\varphi \overline{v\theta}}{\partial \varphi} - \frac{\partial \overline{\omega\theta}}{\partial p} + \overline{Q}, \qquad (16)$$

in which φ is the latitude, v is the meridional wind, ω the vertical pressure velocity, θ is the potential temperature, Q is the diabatic heating, and the overbar denotes zonal average. Upon vertical integration from the surface (p_s) to the tropopause (p_t), the vertical transport term on the
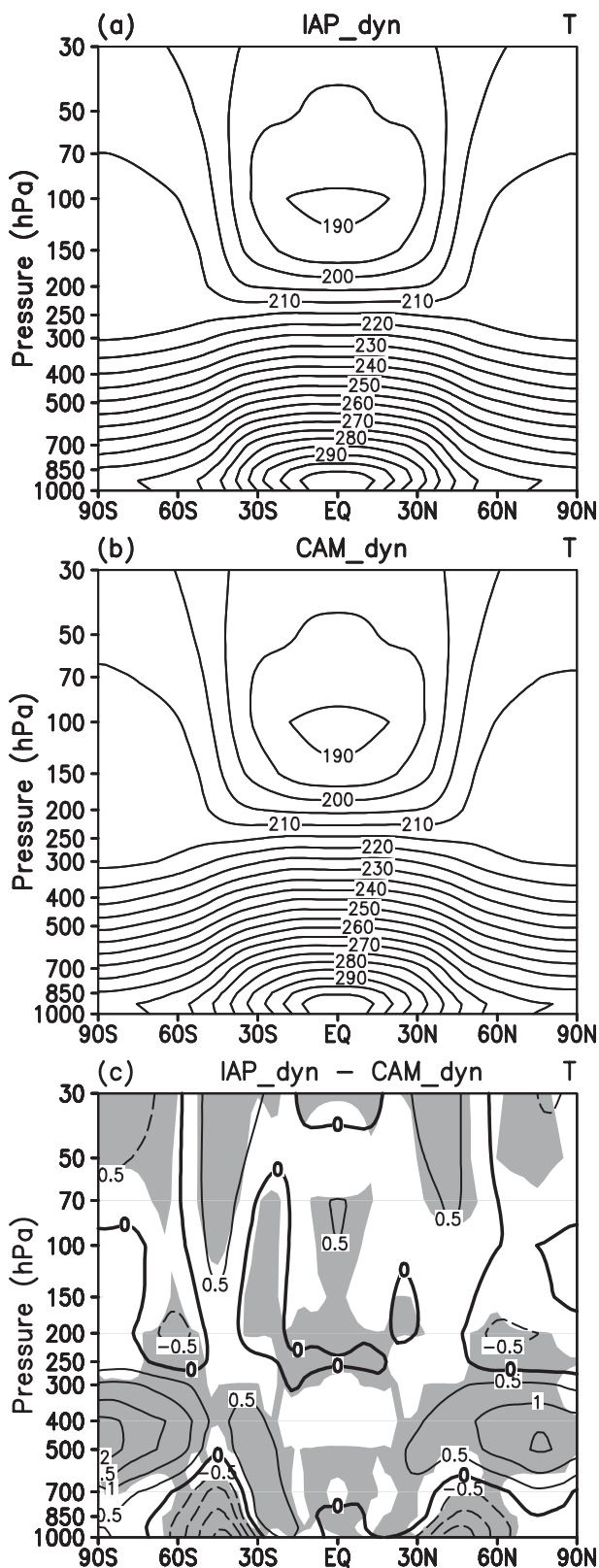
FIG. 7. Zonally averaged 17-period mean temperature from the H–S tests with the (a) IAP and (b) CAM dynamical cores, and (c) their difference (IAP − CAM). Contour intervals are 5 K in (a),(b) and 0.5 K in (c).
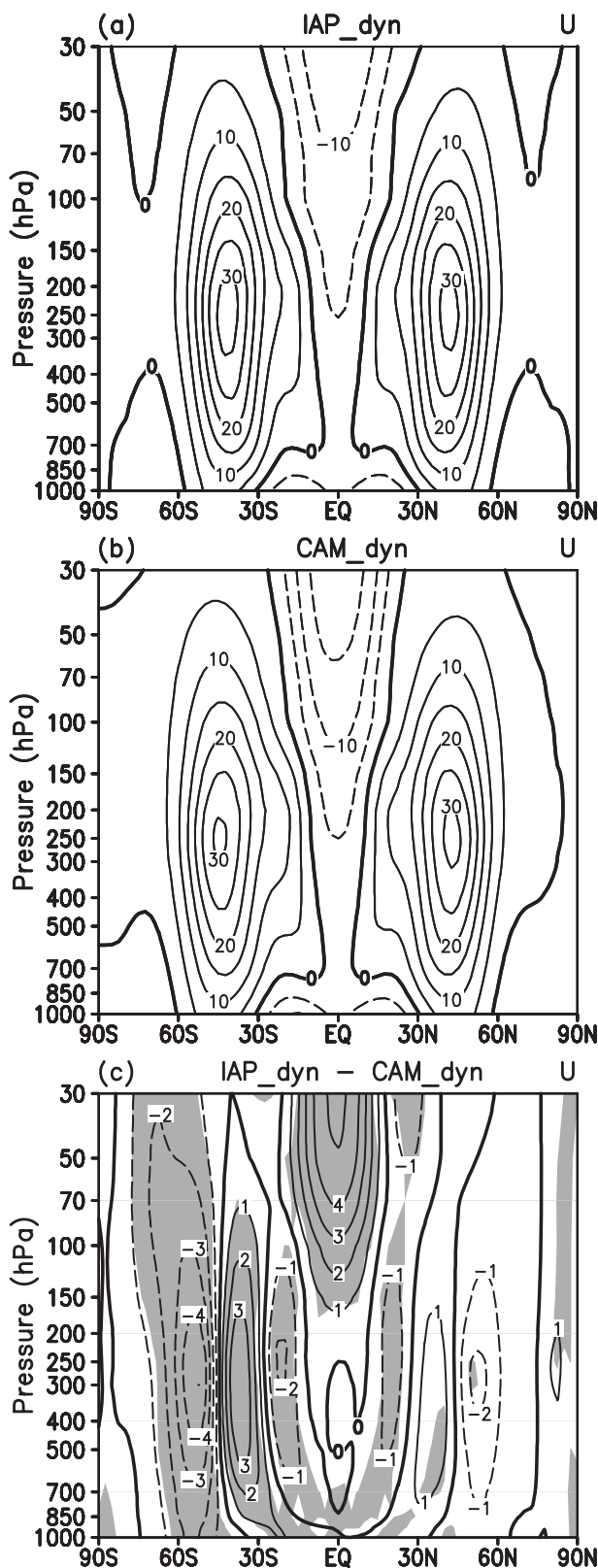
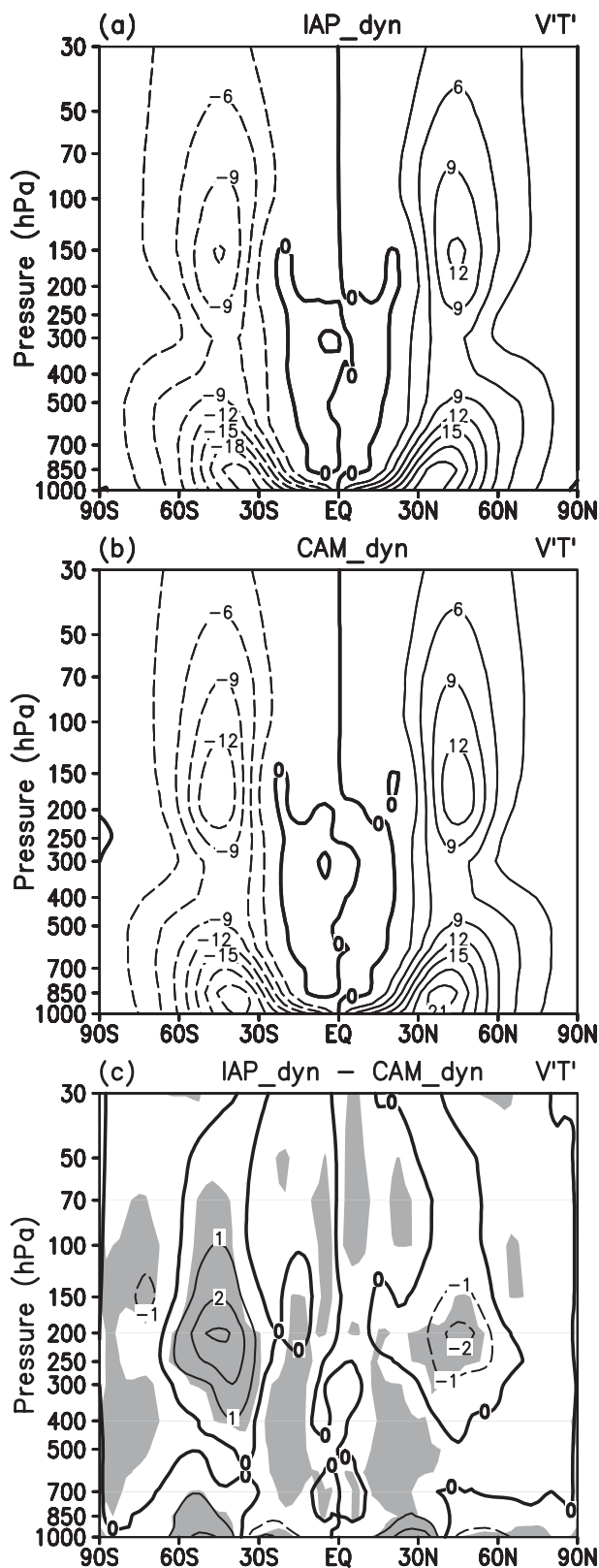FIG. 8. As in Fig. 7, but for zonal wind. Contour intervals are (a),(b) 5 m s^{-1} and (c) 1 m s^{-1}.

FIG. 9. As in Fig. 7, but for transient eddy heat flux. Contour intervals are (a),(b) 3 K m s^{-1} and (c) 1 K m s^{-1}.
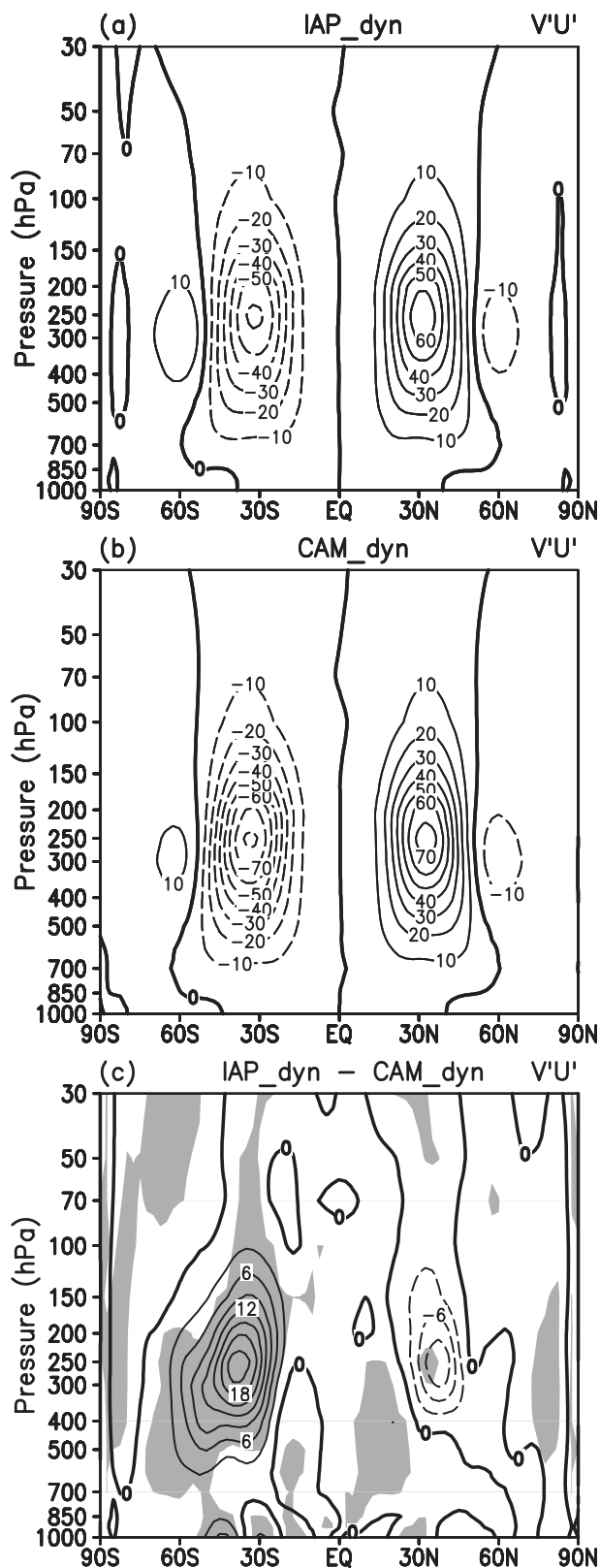
FIG. 10. As in Fig. 7, but for transient eddy momentum flux. Contour intervals are (a),(b) 10 m^2 s^{-2} and (c) 3 m^2 s^{-2}.
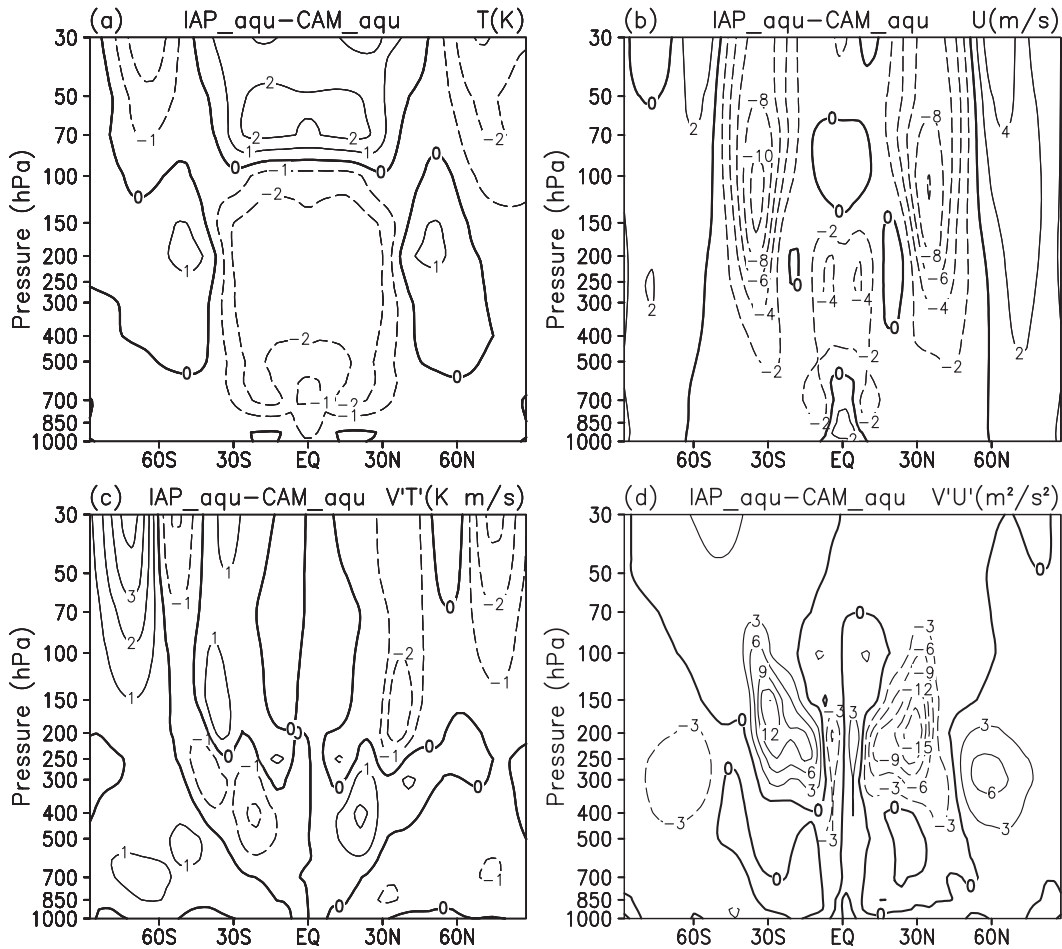
FIG. 11. The difference of zonally averaged annual mean between IAP and CAM from aquaplanet tests: (a) temperature, (b) zonal wind, (c) transient eddy heat flux, and (d) transient eddy momentum flux. Contour intervals are 1 K in (a), 2 m s^{-1} in (b), 1 K m s^{-1} in (c), and 3 m^2 s^{-2} in (d).

right-hand side drops out. Using the quasigeostrophic approximation of meridional transport as in Andrews et al. (1987, 123–133), we have

$$\int_{P_t}^{p_s} \overline{v\theta}\, dp = \int_{P_t}^{p_s} \overline{v}\,\overline{\theta}\, dp + \int_{P_t}^{p_s} \overline{v'\theta'}\, dp$$

$$\approx \int_{P_t}^{p_s} \overline{v}_g \overline{\theta}\, dp + \int_{P_t}^{p_s} \overline{v'\theta'}\, dp = \int_{P_t}^{p_s} \overline{v'\theta'}\, dp \quad (17)$$

because the zonal average of the geostrophic velocity of meridional wind $\overline{v}_g$ is zero. For the dry model, Q is specified as a relaxation to the radiative equilibrium temperature $\overline{\theta}_e$, which can be schematically written as

$$\overline{Q} = -\alpha(\overline{\theta} - \overline{\theta}_e), \quad (18)$$

where α is a relaxation coefficient. Substituting Eqs. (17) and (18) into Eq. (16) and integrating over the tropics from the equator to latitude φ_1 (say, 30°N), we

get the following steady-state relationship between low-latitude temperature and eddy transport after some rearrangements:

$$\frac{1}{\cos\varphi_1} \int\int_{\varphi=0,\varphi_1;p} (\alpha\overline{\theta})a\cos\varphi\, d\varphi\, dp$$

$$= \frac{1}{\cos\varphi_1} \int\int_{\varphi=0,\varphi_1;p} (\alpha\overline{\theta}_e)a\cos\varphi\, d\varphi\, dp - \int_p \overline{v'\theta'}\Big|_{\varphi_1} dp.$$

$$(19)$$

In the IAP dry model, the last term on the right-hand side is smaller than that in the CAM3.1 because of weaker eddy activities. This explains why the IAP core simulated a warmer troposphere in low latitudes relative to the CAM core.

When moist physics is included with topography, the diabatic heating is no longer in the simple form of Eq. (18). The weak eddies with the IAP dynamic core can lead to weaker transport not only in heat, but also in

(a) IAP_full   Q transport

(b) CAM_full   Q transport

(c) IAP − CAM   Q transport
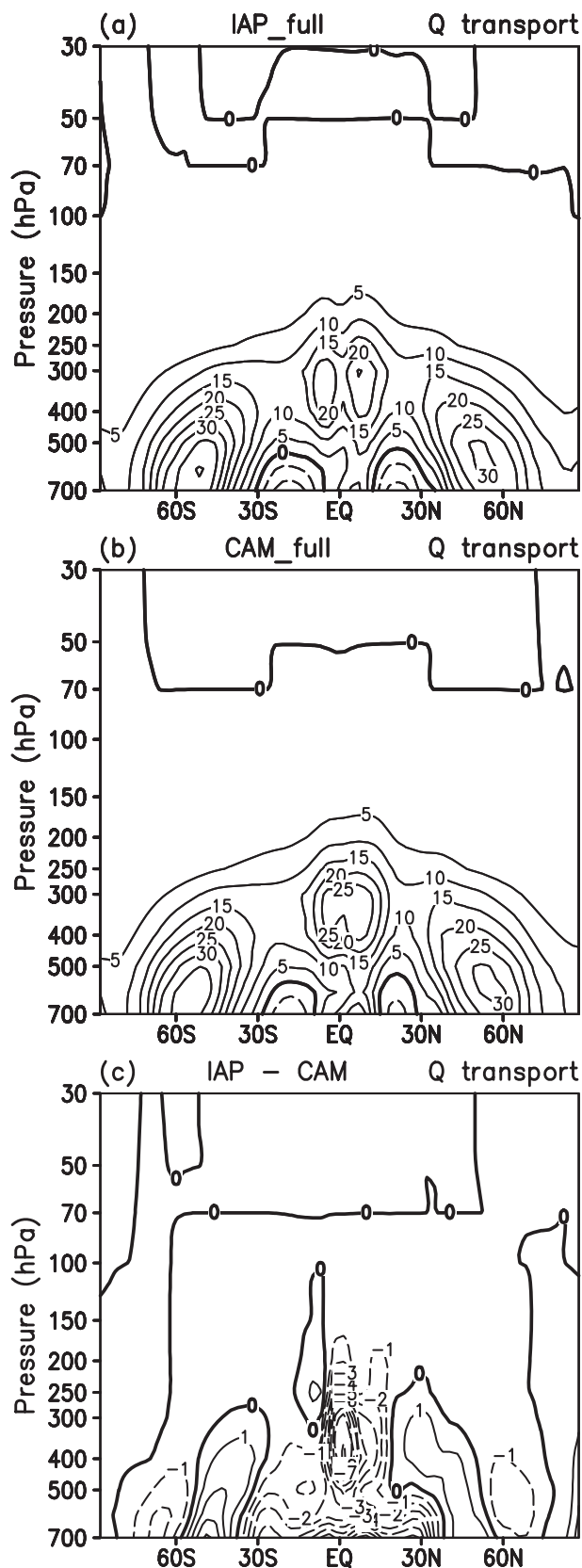
moisture. Figures 12a,b show the three-dimensional transport tendencies of water vapor in the two models. Because water vapor decreases exponentially with height, only values in the middle and upper troposphere are shown. Upward and poleward transport of water vapor are seen in both models. Figure 12c shows the difference between the two models. It is seen that the transport is systematically weaker in the model with the IAP dynamical core.

This difference leads to a systematic difference in the relative humidity in the two models (Fig. 13), which leads to difference in clouds as shown in Fig. 14. The IAP dynamical core is drier than the CAM3.1 core, especially in the upper troposphere. The reduction of cloud amount in the upper troposphere reaches about 20% of the mean cloud amount. High clouds are greenhouse agents that trap infrared radiation to space. The smaller amount of high clouds in the IAP model corresponds to a cooling difference relative to the CAM model. This is shown in Fig. 15 for the total radiative cooling rate (sum of longwave radiative heating qrl and shortwave radiative heating qrs) in the IAP model (Fig. 15a), the CAM (Fig. 15b), and the difference (Fig. 15c). There is larger upper-tropospheric radiative cooling in the IAP model than in the CAM in Fig. 15c, which corresponds well with the smaller amount of high clouds in the IAP model shown in Fig. 14c.

To demonstrate that it is indeed the clouds that caused the difference in the radiative heating, we carried out a series of offline radiation calculations. The purpose of the calculation is to compute longwave (shortwave) fluxes as well as heating rates at every pressure level. The major inputs include specific humidity, temperature, cloud fraction, cloud liquid water path, and ozone mixing ratios, and the outputs include longwave (shortwave) heating rates and longwave (shortwave) upward and downward fluxes. The set of calculations is listed in Table 1. For simplicity, we used the annual mean fields from climate simulation in the two moist models as inputs in the offline calculations. Figure 16a gives radiative heating difference between the offline calculations using the IAP and the CAM model output. The difference pattern is consistent with that in Fig. 15c. There is a larger radiative cooling in most region of troposphere in IAP moist model compared to the CAM

←

FIG. 12. Zonally averaged annual mean dynamical transport of moisture from (a) IAP and (b) CAM full-physics experiments with realistic boundary conditions, and (c) their difference (IAP − CAM). Contour intervals are 5×10^{-2} g kg^{-1} day^{-1} in (a),(b) and 1×10^{-2} g kg^{-1} day^{-1} in (c).
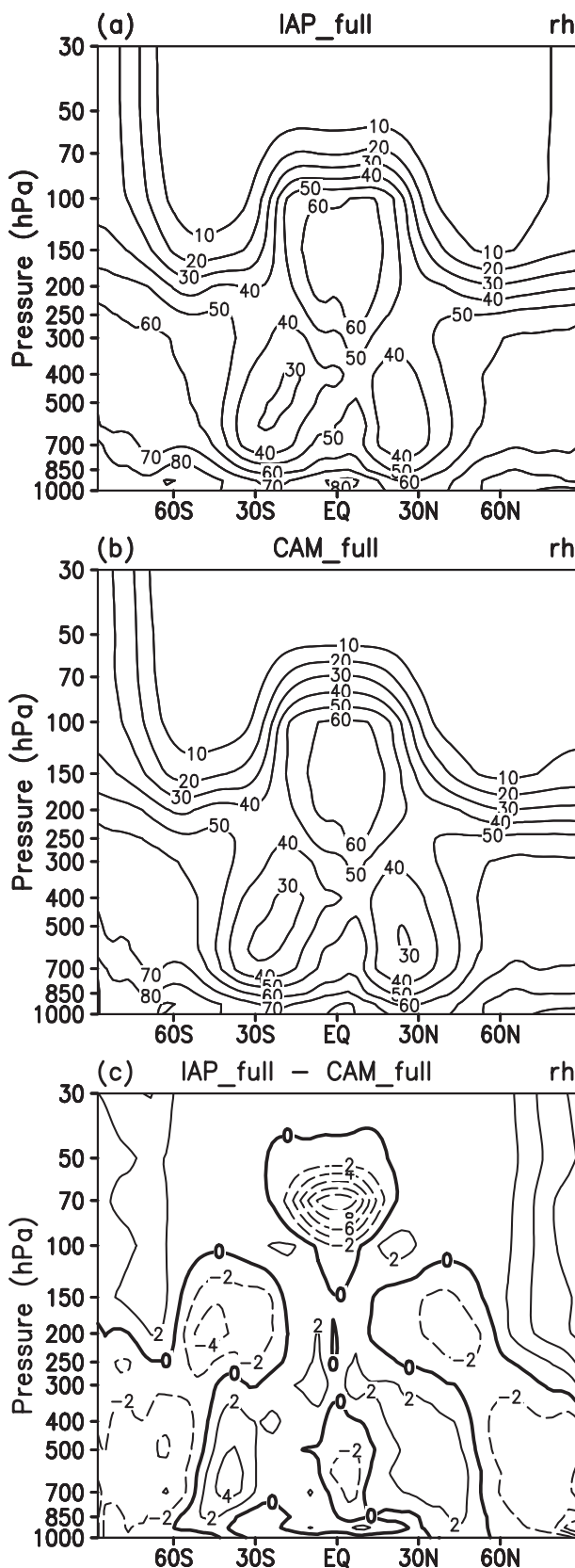
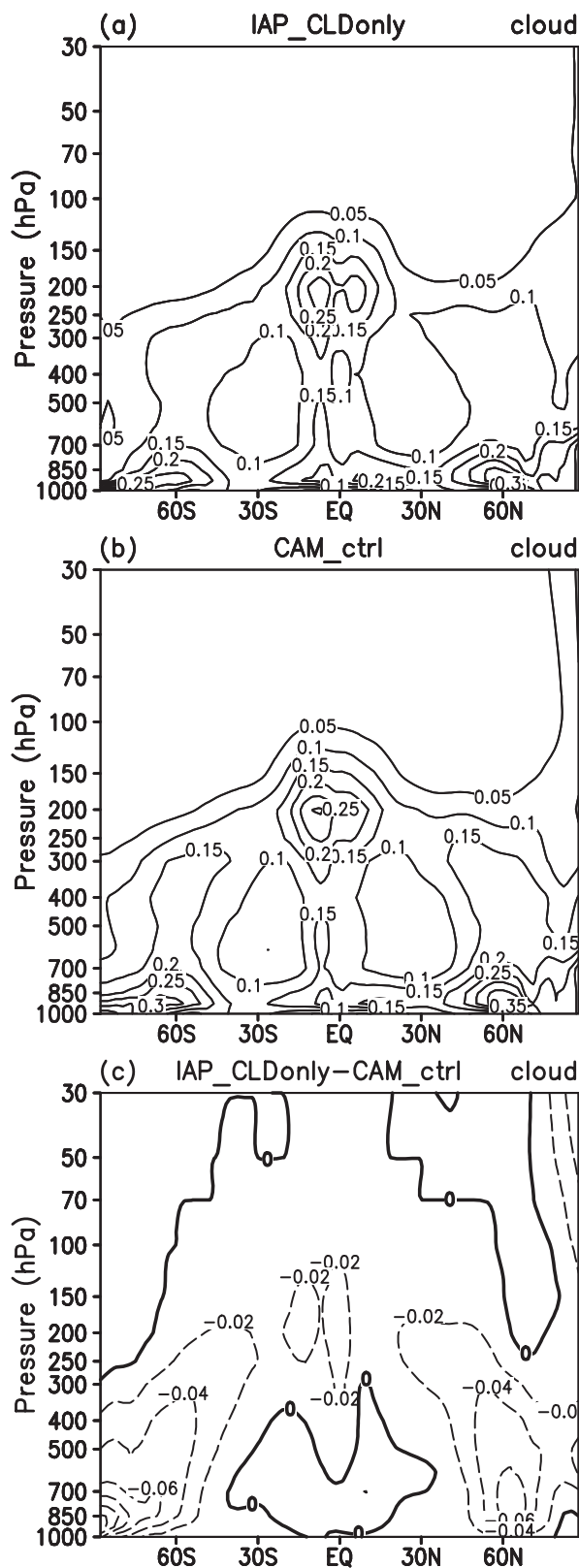FIG. 13. As in Fig. 11, but for relative humidity. Contour intervals are (a),(b) 10% and (c) 2%.

FIG. 14. Cloud fraction used in experiment (a) IAP_CLDonly and (b) CAM_ctrl, and (c) their difference (IAP_CLDonly − CAM_ctrl). Contour intervals are 0.05 in (a),(b) and 0.02 in (c).
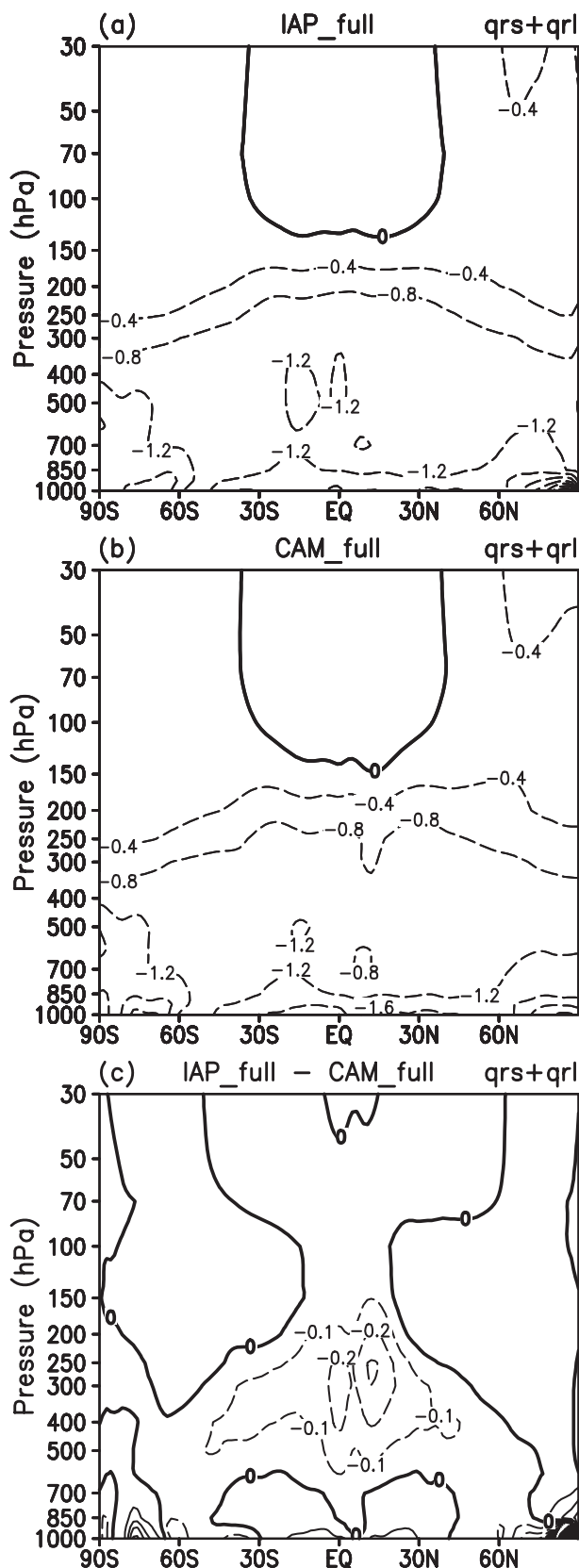
TABLE 1. Input fields of offline radiation calculations. The fields with suffix CAM are 15-yr annual mean outputs from climate simulation with CAM, while the fields with suffix IAP are outputs from the IAP model.

Expt name	Temperature	Specific humidity	Cloud fraction
	Sensitivity input fields		
CAM_ctrl	T_CAM	Q_CAM	CLD_CAM
IAP_ctrl	T_IAP	Q_IAP	CLD_IAP
IAP_CLDonly	T_CAM	Q_CAM	CLD_IAP
IAP_Tonly	T_IAP	Q_CAM	CLD_CAM
IAP_Qonly	T_CAM	Q_IAP	CLD_CAM

moist model. Figure 16b shows the difference of heating rate due to change of clouds. It is seen that cloud fraction is the dominant contributor to the different radiative cooling between the two moist models, while temperature and water vapor have much smaller contributions (Figs. 16c,d). In addition to the radiative heating, the diabatic heating term in the thermodynamic equation [Eq. (16)] also contributes to the latent heat and turbulent transport including convection (not shown). But these are found to be opposite to the difference in the total diabatic heating between the two models.

The impact of diabatic heating on the difference between the dry model and full model can be further illustrated with Fig. 17, which gives a segment of the time evolution of the temperature tendency, and the contributions from dynamics and diabatic heating with the IAP core, in Fig. 17a for the dry H–S simulation and in Fig. 17b for the moist model. Here the diabatic heating is calculated from physical parameterizations in the models, and the dynamical tendency, representing the adiabatic heating from transport, is derived by total temperature tendency minus the diabatic heating. The frictional heating and the heating from energy fixer are classified to the diabatic heating, which are found to be small. It is seen that in the H–S test, the total temperature tendency closely follows the dynamical term. The variation of the contribution from the diabatic heating is smaller than that of the dynamical terms. Its maximum has a time lag to the minimum in the total tendency. There is no significant correlation between adiabatic heating and dynamic tendency. However, in the moist

←

FIG. 15. Zonally averaged annual mean radiative diabatic heating (qrs and qrl for shortwave and longwave radiative heating, respectively) rate from (a) IAP and (b) CAM simulations, and (c) their difference (IAP − CAM). Contour intervals are 0.4 K day^{-1} in (a),(b) and 0.1 K day^{-1} in (c).
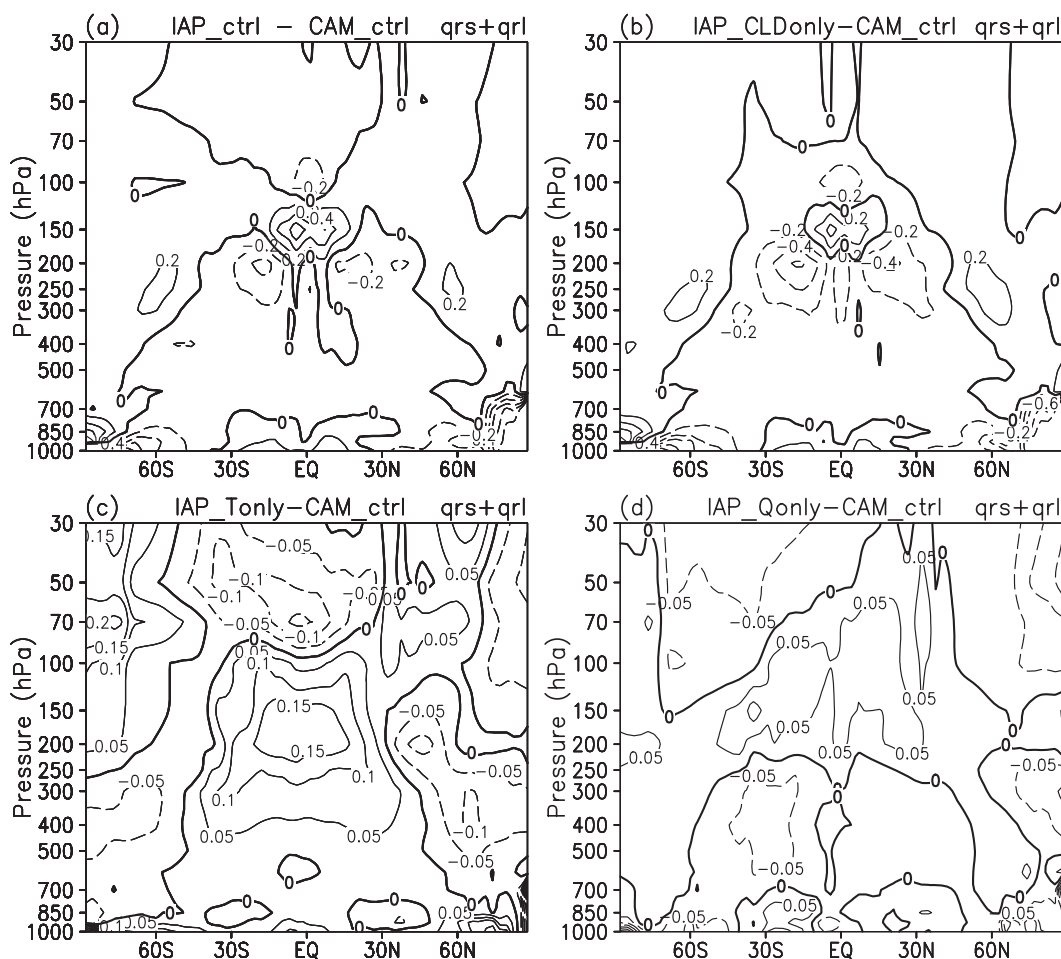
FIG. 16. Differences of radiative diabatic heating rate from the sensitivity experiments: (a) IAP_ctrl − CAM_ctrl, (b) IAP_CLDonly − CAM_ctrl, (c) IAP_Tonly − CAM_ctrl, and (d) IAP_Qonly − CAM_ctrl. Contour intervals are 0.2 K day^{-1} in (a),(b) and 0.05 K day^{-1} in (c),(d).

model, there is significant negative correlation between adiabatic heating and the dynamic term. Namely, if there is a warming due to dynamic transport, there is an offsetting diabatic heating that quickly responds to cool the atmosphere. The variation of the diabatic heating is comparable to or can overcompensate that from the dynamical transport in driving the temperature variation.

4. Summary

The zonal mean temperature, wind, and eddy fluxes in climate simulations with the IAP dynamical core and the Eulerian spectral transform CAM3.1 dynamical core are evaluated. The results reveal that the tropospheric temperature in the IAP model with full physics is colder than that in the CAM3.1 (and closer to the NCEP–NCAR reanalysis) in low and midlatitudes. But when the dynamical

core is used in dry simulation, the IAP model simulated a warmer troposphere than the CAM3.1. Aquaplanet experiments are used to rule out the impact of different treatment of topography as the cause of the difference between the two models with full physics.

We have shown that the IAP dynamical core simulated less energetic eddies relative to the CAM3.1. These are consistent among the experiments of dry and moist atmospheres and on aquaplanets. In the dry simulation, the less energetic eddies correspond to smaller heat transport to polar regions, which leads to the warmer troposphere in the IAP model. In the moist simulation, however, the less energetic eddies also cause less upward transport of water vapor, and less high cloud amount in the IAP model. The reduced high clouds correspond to increased radiative cooling of the atmosphere in the IAP model, leading to a colder troposphere relative to CAM3.1.
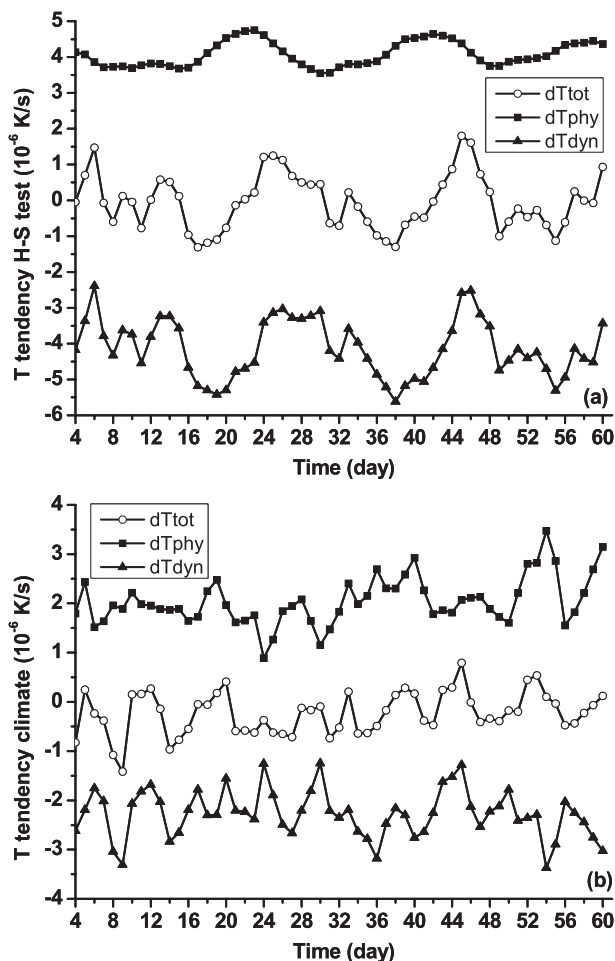
FIG. 17. Evolution of heating rate from the IAP model in (a) H–S test and (b) climate simulation in troposphere (150–1000 hPa) at low latitude (30°S–30°N). Solid square: diabatic heating rate, solid triangle: adiabatic heating rate, and hollow circle: total heating rate. Unit: 10^{-6} K s^{-1}.

Our study demonstrates how interactive moist physics, especially clouds, can change the behavior of a dynamical core in climate models. It points to the need to understand dynamical cores both in isolation and with full physics. To our knowledge, this is the first effort to report and analyze the cause of the opposite impact of dynamical core between dry and moist models on climate simulations.

REFERENCES

Andrews, D. G., J. R. Holton, and C. B. Leovy, 1987: *Middle Atmosphere Dynamics.* Academic Press, 489 pp.

Arakawa, A., and V. B. Lamb, 1977: Computational design of the basic dynamical process of the UCLA general circulation model. *Methods in Computational Physics,* J. Chang, Ed., Vol. 17, Academic Press, 173–265.

Baba, Y., K. Takahashi, T. Sugimura, and K. Goto, 2010: Dynamical core of an atmospheric general circulation model on a Yin–Yang grid. *Mon. Wea. Rev.,* **138,** 3988–4005.

Bi, X., 1993: IAP 9L AGCM and climate simulation (in Chinese). Ph.D. dissertation, Institute of Atmospheric Physics, Chinese Academy of Sciences, 210 pp.

Boer, G. J., and B. Denis, 1997: Numerical convergence of the dynamics of a GCM. *Climate Dyn.,* **13,** 359–374.

——, and Coauthors, 1992: Some results from an intercomparison of the climates simulated by 14 atmospheric general circulation models. *J. Geophys. Res.,* **97** (D12), 12 771–12 786.

Charney, J. G., 1971: Geostrophic turbulence. *J. Atmos. Sci.,* **28,** 1087–1095.

Chen, H., Z. Lin, and G. Zhou, 2004: Experimental dynamical prediction of spring dust storm events in China (in Chinese). *Climatic Environ. Res.,* **9,** 182–190.

Collins, W. D., and Coauthors, 2004: Description of the NCAR Community Atmosphere Model (CAM3.0). NCAR Tech. Note NCAR/TN-464+STR, 214 pp.

Decker, M., M. A. Brunke, Z. Wang, K. Sakaguchi, X. Zeng, and M. G. Bosilovich, 2012: Evaluation of the reanalysis products from GSFC, NCEP, and ECMWF using flux tower observations. *J. Climate,* **25,** 1916–1944.

Dee, D. P., and Coauthors, 2011: The ERA-Interim Reanalysis: Configuration and performance of the data assimilation system. *Quart. J. Roy. Meteor. Soc.,* **137,** 553–597.

Donner, L. J., and Coauthors, 2011: The dynamical core, physical parameterizations, and basic simulation characteristics of the atmospheric component AM3 of the GFDL Global Coupled Model CM3. *J. Climate,* **24,** 3484–3519.

Ghan, S. J., J. W. Lingaas, M. E. Schlesinger, R. L. Mobley, and W. L. Gates, 1982: A documentation of the OSU two-level atmospheric general circulation model. Oregon State University Climatic Research Institute Rep. Issue 35, 395 pp.

Giraldo, F. X., and M. Restelli, 2008: A study of spectral element and discontinuous Galerkin methods for the Navier–Stokes equations in nonhydrostatic mesoscale atmospheric modeling: Equation sets and test cases. *J. Comput. Phys.,* **227,** 3849–3877.

Held, I. M., and M. J. Suarez, 1994: A proposal for the intercomparison of the dynamical cores of atmospheric general circulation models. *Bull. Amer. Meteor. Soc.,* **75,** 1825–1830.

Jablonowski, C., and D. L. Williamson, 2006: Baroclinic wave test case for dynamical cores of GCMs. *Quart. J. Roy. Meteor. Soc.,* **132,** 2943–2976.

Kalnay, E., and Coauthors, 1996: The NCEP/NCAR 40-Year Reanalysis Project. *Bull. Amer. Meteor. Soc.,* **77,** 437–471.

Liang, X., 1996: Description of a nine-level grid point atmospheric general circulation model. *Adv. Atmos. Sci.,* **13,** 269–298.

Lin, Z., and Q. Zeng, 1997: Simulation of East Asian summer monsoon by using an improved AGCM. *Adv. Atmos. Sci.,* **14,** 513–526.

Neale, R. B., and B. J. Hoskins, 2000: A standard test for AGCMs including their physical parameterizations: I: The proposal. *Atmos. Sci. Lett.,* **1,** 101–107.

Phillips, N. A., 1957: A coordinate system having some special advantages for numerical forecasting. *J. Meteor.,* **14,** 184–185.

Polvani, L. M., R. K. Scott, and S. J. Thomas, 2004: Numerically converged solutions of the global primitive equations for testing the dynamical core of atmospheric GCMs. *Mon. Wea. Rev.,* **132,** 2539–2552.

Rayner, N. A., and Coauthors, 2003: Global analyses of sea surface temperature, sea ice, and night marine air temperature since the late nineteenth century. *J. Geophys. Res.,* **108,** 4407, doi:10.1029/2002JD002670.

Reynolds, R. W., N. A. Rayner, T. M. Smith, D. C. Stokes, and W. Wang, 2002: An improved in situ and satellite SST analysis for climate. *J. Climate,* **15,** 1609–1625.

Ringler, T. D., D. Jacobsen, M. Gunzburger, L. Ju, M. Duda, and W. Skamarock, 2011: Exploring a multiresolution modeling approach within the shallow-water equations. *Mon. Wea. Rev.,* **139,** 3348–3368.

Taylor, M. A., J. Edwards, and A. St-Cyr, 2008: Petascale atmosphere models for the Community Climate System Model: New developments and evaluation of scalable dynamical cores. *J. Phys.: Conf. Ser.,* **125,** 012023, doi:10.1088/1742-6596/125/1/012023.

Tomita, H., and M. Satoh, 2004: A new dynamical framework of nonhydrostatic global model using the icosahedral grid. *Fluid Dyn. Res.,* **34,** 357–400.

Umscheid, L., and M. Sankar-Rao, 1971: Further tests of a grid system for global numerical prediction. *Mon. Wea. Rev.,* **99,** 686–690.

Wan, H., M. A. Giorgetta, and L. Bonaventura, 2008: Ensemble Held-Suarez test with a spectral transform model: Variability, sensitivity, and convergence. *Mon. Wea. Rev.,* **136,** 1075–1092.

Washington, W. M., and A. Kasahara, 1970: A January simulation experiment with the two-layer version of the NCAR global circulation model. *Mon. Wea. Rev.,* **98,** 559–580.

Williamson, D. L., 2002: Time-split versus process-split coupling of parameterizations and dynamical core. *Mon. Wea. Rev.,* **130,** 2024–2041.

——, 2007: The evolution of dynamical core for global atmospheric models. *J. Meteor. Soc. Japan,* **85B,** 241–269.

——, 2008: Equivalent finite volume and Eulerian spectral transform horizontal resolutions established from aqua-planet simulations. *Tellus,* **60A,** 839–847.

——, and P. J. Rasch, 1989: Two-dimensional semi-Lagrangian transport with shape-preserving interpolation. *Mon. Wea. Rev.,* **117,** 102–129.

Xue, F., X. Bi, and Y. Lin, 2001: Modelling the global monsoon system by IAP 9L AGCM. *Adv. Atmos. Sci.,* **18,** 404–412.

Zeng, Q., and Coauthors, 1989: Documentation of IAP two-level atmospheric general circulation model. Department of Energy Tech. Rep. DOE/ER/60314-H1 TR044, 383 pp.

——, and Coauthors, 1997: Seasonal and extraseasonal predictions of summer monsoon precipitation by GCMs. *Adv. Atmos. Sci.,* **14,** 163–176.

Zhang, H., 2009: Development of IAP atmospheric general circulation model version 4.0 and its climate simulations (in Chinese). Ph.D. dissertation, Institute of Atmospheric Physics, Chinese Academy of Sciences, 194 pp.

——, Z. Lin, and Q. Zeng, 2009: The computational scheme and the test for dynamical framework of IAP AGCM-4 (in Chinese). *Chinese J. Atmos. Sci.,* **33,** 1267–1285.

Zuo, R., 2003: Development of new generation grid point atmospheric general circulation model with high resolution (in Chinese). Ph.D. dissertation, China People's Liberation Army University of Science and Technology, 328 pp.

——, and Coauthors, 2004: Designing and climatic numerical modeling of 21-level AGCM (IAP AGCM-III). Part I: Dynamical framework (in Chinese). *Chinese J. Atmos. Sci.,* **28,** 659–674.